Bimetallic Fe-Mo sulfide/carbon nanocomposites derived from phosphomolybdic acid encapsulated in MOF for efficient hydrogen generation

Zheng Huang [a], Zhuxian Yang [a], Mian Zahid Hussain [a], Quanli Jia [b], Yanqiu Zhu [a], Yongde Xia [a,*]

[a] *College of Engineering, Mathematics and Physical Sciences, University of Exeter, Exeter EX4 4QF, UK*

[b] *Hennan Key Laboratory of High Temperature Functional Ceramics, Zhengzhou University, Zhengzhou, 450052, China*

* Corresponding author.

Email address: y.xia@exeter.ac.uk (Y. Xia).

ABSTRACT

To tackle the energy crisis and achieve a more sustainable development, hydrogen as a clean and renewable energy resource has attracted great interest. Searching for cheap but efficient catalysts for hydrogen production from water splitting is urgently needed. In this report, bimetallic Fe-Mo sulfide/carbon nanocomposites that derived from a polyoxometalate phosphomolybdic acid encapsulated in metal organic framework MIL-100 (PMA@MIL-100) have been generated and their applications in electrocatalytic hydrogen generation were explored. The PMA@MIL-100 precursor is formed via a simple one-pot hydrothermal synthesis method and the bimetallic Fe-Mo sulfide/carbon nanocomposites were obtained by chemical vapour sulfurization of PMA@MIL-100 at high temperatures. The nanocomposite samples were fully characterized by a series of techniques including XRD, FT-IR, TGA, N_2 gas sorption, SEM, TEM, XPS, and were further investigated as electrocatalysts for hydrogen production from water splitting. The hydrogen production activity of the best performed bimetallic Fe-Mo sulfide/carbon nanocomposite exhibits an overpotential of -0.321 V at 10 mA cm^{-2} and a Tafel slope of 62 mV dec^{-1} with a 53% reduction in overpotential compared to Mo-free counterpart composite. This dramatic improvement in catalytic performance of the Fe-Mo sulfide/carbon composite is attributed to the homogeneous distribution of the nanosized iron sulfide, MoS_2 particles and the formation Fe-Mo-S phases in the S-doped porous carbon matrix. This work has demonstrated a potential approach to fabricate complex heterogeneous catalytic materials for different applications.

KEYWORDS: MOF; nanocomposite; encapsulation; metal sulfide; hydrogen generation

1. Introduction

The fast-growing global energy consumption has urged the development of novel and sustainable alternative energy solutions. Hydrogen (H_2) has become the most promising, zero-emission clean energy due to its huge and easy accessible reserves. However, to realise the use of H_2 as a clean energy, four obstacles including the efficient production, ways of storage, means of utilization and the safety control of hydrogen must be overcome.[1] To effective produce hydrogen, one of the most simple but important approaches is electrolysis of water via hydrogen evolution reaction (HER), which is the cathodic half reaction of water splitting. To bring the produced clean H_2 energy into large-scale practical utilisation, it is pivotal to develop cost-effective and stable electrocatalysts that can lower the overpotential required for this reaction, improve the energy efficiency, consequently to realise the effective materials for hydrogen production. Pt-based material is currently the benchmark catalyst towards HER for water splitting in acidic media. It is highly active and shows high current densities at low overpotentials, but its scarcity and high price has prohibited it from large scale applications. Therefore, it is highly desirable to develop non-precious metal based materials which are efficient for HER.[2]

Actually, a growing amount of heterogeneous catalysts have emerged under this circumstance in the past years.[3] In particular, MoS_2 has shown great potential as a promising electrocatalyst for HER.[4] Initially, bulk MoS_2 was considered as an inactive catalysts due to the extremely high hydrogen adsorption free energy ((ΔG_H) of 1.92 eV at its basal plane.[5] It was later proved by both theoretical simulations and experimental discoveries that the metallic edge sites of the MoS_2 (i.e. Mo-edge) are active in HER for water splitting.[6, 7] With the ΔG_H close to zero,[8] the amount of edge sites exposed in MoS_2 significantly increased, which results in enhanced electrocatalytic HER activity of the material. Indeed, significant progress

has been made in this exciting field that abundant edge-exposed nanostructured MoS_2 has been developed to achieve better electrocatalytic HER performance.[3]

Moreover, the catalytic activity of MoS_2 can be further improved via activation of the theoretically inactive basal plane and its S-edge. Report has suggested that incorporating transition metal ions such as Co, Ni and Fe into the edge sites can reduce the ΔG_H of the S-edge, therefore improve its electrocatalytic HER activity.[9] Meanwhile, doping metal ions such as Co^{2+} or Zn^{2+} into MoS_2 in-plane can decrease the electron number of the S atom to compensate the mismatching of the energy levels, thus enhance the adsorption of H and increase the HER activity.[10, 11] Hakala et al. carried out DFT calculations and found that in-plane doping of MoS_2 with Fe, Co, Ni, Cu, Pd and Pt could bring the ΔG_H of the MoS_2 at S sites towards the optimal adsorption condition, which could be beneficial to electrochemistry applications.[12] On the other hand, iron sulfide based materials including FeS,[13] FeS_2, Fe_3S_4, Fe_9S_{10} [14] and Fe_7S_8 [15] have shown electrocatalytic activity for HER in water splitting. Therefore some composites such as FeS_2@MoS_2/rGO,[16] Fe-MoS_2,[17] Fe-MoS_2 nanoflower,[18] $Fe_{1-x}S$/MoS_2 [19] and FeS@MoS_2/CFC [20] have been further developed and shown great potential in electrochemical energy applications.

Metal-organic frameworks (MOFs) are porous crystalline materials which have numerous potential applications in adsorption, separation and catalysis due to their high surface areas and large pore volumes, tailorable structures, and promising hosts to stabilize and encapsulate large guest molecules/clusters. Actually, since the first report of the encapsulation of polyoxometalates (POM) within MIL-101 cages in 2005,[21] the incorporation of large guest clusters such as POM inside porous MOFs (POM@MOFs) has been a common strategy to prepare highly dispersed active species useful for catalytic applications and further functionalization.[22] In particular, to effective encapsulate large clusters like phosphomolybdic acid (PMA), a molybdenum-based compounds containing heteropoly acid

that forms kegging type polyatomic ion with diameter of 13 Å in water [23] into porous substrates, an iron-containing MOF MIL-100, is a promising host since it contains two types of confined pores with diameters of 25 and 29 Å and corresponding pore apertures of 5.5 and 8.6 Å respectively,[24] which is ideal for PMA immobilization. This type of PMA@MOF guest/host composites are excellent precursors to provide sources of metal ions and carbon species simultaneously. They can be readily transform to catalytic active species like electrocatalytic active metal component nanoparticles embedded in porous carbon substrates via a high temperature pyrolysis process under controlled gas atmospheres,[25-30] which offer an alternative approach to develop new nanomaterials that are efficient in environmental and energy applications but difficult to generate via traditional material fabrication processes. Frequently, the generated nanocomposites are mainly transition metal oxides or carbides nanoparticles uniformly distributed on porous carbons and exhibited much increased electrocatalytic performance.[25-28, 31] These improvements are mainly due to the effective minimization of the agglomeration of the electrocatalytic active metal components nanoparticles as well as the remarkably increased electronic conductivity of the nanocomposites by the in-situ formed porous carbon substrates.[26, 31]

Herein we endeavour to generate dual metallic Fe-Mo sulfide@carbon nanocomposites using a one-pot hydrothermal synthesized phosphomolybdic acid (PMA) encapsulated in MIL-100 (PMA@MIL-100) as a precursor. High temperatures chemical vapour sulfurization of PMA@MIL-100 in H_2S atmosphere results in the formation of bimetallic Fe-Mo sulfide/carbon nanocomposites in which the Fe-Mo sulfide nanoparticles are uniformly distributed in the in-situ formed porous carbons. The resulting Fe-Mo sulfide/porous carbon nanocomposites exhibit good electrocatalytic activity for hydrogen generation from water splitting.

2. Experimental

2.1. Materials

All reagents were purchased from Fisher Scientific and used without further purification. Iron (III) chloride anhydrous ($FeCl_3$, ≥ 98%), Trimethyl-1, 3, 5-benzenetricarboxylate ($C_6H_3(CO_2CH_3)_3$, 99%, abbreviated as Me3btc), Phosphomolybdic acid hydrate ($H_3PMo_{12}O_{40}\cdot xH_2O$, abbreviated as PMA).

2.2. Samples preparation

Synthesis of MIL-100: MIL-100(Fe) was synthesized according to previous report.[32] 0.694 g (2.75 mmol) of Trimethyl-1, 3, 5-benzenetricarboxylate was first dispersed in 25 ml of H_2O, then 0.811 g of $FeCl_3$ was added and dissolved in the same solution. This mixture solution was then transferred to a Teflon lined stainless steel autoclave and placed in an oven at 130 °C for 72 hrs, followed by cooling the autoclave naturally down to room temperature. The orange powder was then collected via centrifugation at 5500 rpm for 5 mins, washed once with water then twice with hot acetone. This collected sample was denoted as MIL-100.

Synthesis of PMA@MIL**:** Similar to the synthesis of pure MIL-100(Fe), 0.694 g of Trimethyl-1, 3, 5-benzenetricarboxylate (Me3btc) and 0.811 g $FeCl_3$ were added in 20 ml of water to form a solution. Then calculated amount of phosphomolybdic acid hydrate (PMA) was first dissolved in 5 ml of water to form another solution, which was then added to the mixture solution containing Me3btc and $FeCl_3$. The resulting mixture was transferred to a Teflon lined stainless steel autoclave and placed in an oven at 130 °C for 72 hrs. The remaining steps are identical to that of pure MIL-100. The as-made PMA@MIL-100 samples were denoted as 1-PMA@MIL, 2-PMA@MIL and 3-PMA@MIL with 150, 250 and 350 mg of PMA used during the synthesis respectively.

Synthesis of metal sulfide/carbon nanocomposites: To obtain the metal sulfide/carbon composites, typically 0.05 g dried 1-PMA@MIL powder was loaded in a ceramic boat and subjected to pyrolysis under H_2S atmosphere in a horizontal flow-through tube furnace. First, the tube in the furnace was flushed with Ar to remove the remaining air inside, followed by heated the furnace at ramp rate of 10 °C/min in continuous Ar flow of 50 mL min^{-1}. After the furnace temperature arrived at the target temperature (600, 800 and 1000°C respectively), H_2S gas flow of 50 mL min^{-1} was introduced together with the Ar flow at the target temperature for 1 hour. Afterwards, H_2S was switched off and the furnace was left to cool down naturally with Ar flow remained. The obtained samples were labelled as xMo@MIL-y, where x represents which parental PMA@MIL was used (for example x = 1 when the sample was derived from 1-PMA@MIL) and y represents the pyrolysis temperature of the PMA@MIL. For example, sample derived from 1-PMA@MIL pyrolyzed at 800 °C is denoted as 1Mo@MIL-800. For comparison, MIL-100 was also pyrolyzed in H_2S at 600, 800 and 1000°C for 1 hour and the resulting samples were labelled as MIL-600, MIL-800 and MIL-1000 respectively.

2.3. Materials characterization

Powder X-ray diffraction (XRD) patterns were obtained with Cu-Kα radiation at 40 mA and 40 kV using Bruker D8 advanced X-ray diffractometer. For Fourier-transform infrared (FT-IR) spectra, samples were prepared by KBr pellet method and were recorded in the wavelength range of 500-1300 cm^{-1} on a Shimadzu IRTracer-100 spectrometer. Thermogravimetric analysis (TGA) was performed on a TA SDT Q600 instrument with target temperature of 800 °C, heating ramp of 10 °C/min and air flow rate of 100 mL min^{-1} under air atmosphere. N_2 gas sorption analysis was carried out on a Quantachrome Autosorb iQ gas sorptometer. Before the actual gas analysis, samples were outgassed under vacuum at 150 °C for 3 h. Brunauer-Emmett-Teller (BET) method was used to calculate the surface area of the samples. Adsorption data in the partial pressure (P/P_0) range of 0.05-0.2 was used for the

calculation the surface area. Total pore volume was determined from the amount of adsorbed N_2 at P/P_0 ca. 0.99. Raman spectra were acquired with excitation laser beam of 532 nm in wavelength on a Renishaw inVia Raman microscope using a 20x objective lens. Helios Nanolab 600i scanning electron microscope/Focused ion beam DualBeam workstation was used to acquire scanning electron microscopy (SEM) images. Samples were splattered with gold to reduce the effects of charging. Transmission electron microscopy (TEM) images were obtained by a JOEL-2100 LaB6 transmission electron microscope. Samples were dispersed in absolute ethanol by sonication for 10 min and were deposited on a holey carbon copper grid.

2.4. Electrocatalytic evaluations

Electrochemistry measurements were carried out on a CHI660E electrochemical workstation at room temperature with a three electrode setup. 0.5 M H_2SO_4 electrolyte, 3 mm glassy carbon working electrode, Ag/AgCl reference electrode as well as Pt wire counter electrode were used in this setup. To prepare the working electrode, 3 mg of powder sample was dispersed in 1 mL of water/ethanol solution plus 5 μL of 5 wt% Nafion solution with the help of ultrasonic bath for about 30 mins. Latter, 5 μL of the fresh suspension was drop-cast onto the ready-polished mirror-finished glassy carbon electrode and left drying naturally before test, the amount of loading was 0.21 mg/cm^2. iR-correction was carried out by using the built-in function in the software with compensation level of 95%. All the potential values in this report were converted to vs. E (RHE) for easy comparison.

3. Results and discussion

3.1. Characterisation of the as-made PMA@MIL-100

The parental PMA@MIL precursor was first synthesized via a simple one-pot hydrothermal method by aging a mixture solution of Trimethyl-1, 3, 5-benzenetricarboxylate (Me3btc), $FeCl_3$ and calculated amount of phosphomolybdic acid hydrate (PMA) in H_2O at 130 ^oC for 72 hours. The as-synthesized PMA@MIL was then subjected to high temperature pyrolysis in H_2S/Ar atmosphere to generate the target Fe-Mo bimetallic sulfide/carbon nanocomposites and the whole process was shown in the schematic diagram in Fig. 1.

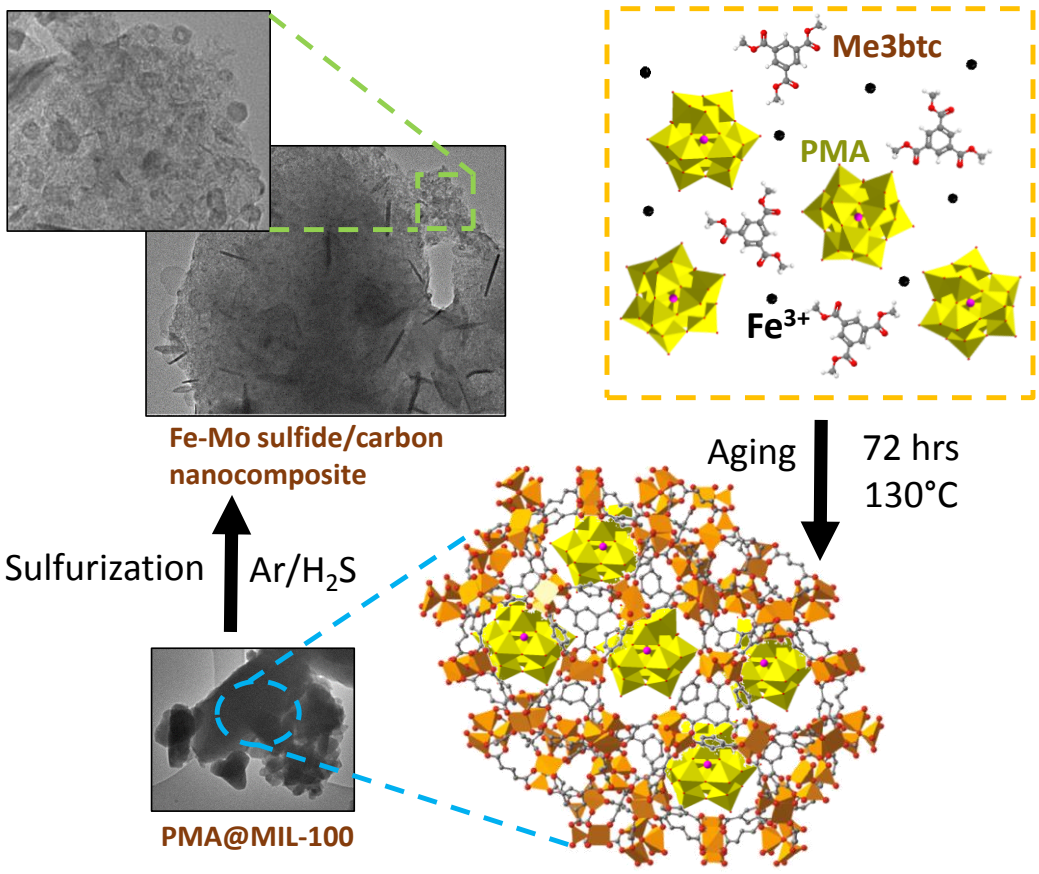

Fig. 1. Schematic diagram of the synthesis of Fe-Mo bimetallic sulfide/carbon composites.

Powder X-ray diffraction (XRD) of all the PMA-containing samples (Fig. S1A) show pronounced MIL-100 characteristic peaks, but the intensity of the characteristic peaks in the range from 3° to 8° decreases or eventually disappears with increase the amount of PMA. Obviously, introducing high amount of PMA into MIL-100 is detrimental to the structures of PMA@MIL composite, which is consistent with previous report.[33] Moreover, no XRD peaks from the PMA were observed regardless of the amount of PMA in the PMA@MIL composite, suggesting that either the amount of PMA in the composite is too small to be detected by XRD or the PMA are fully confined in the pores of MIL-100 and completely shielded from the X-ray. FT-IR spectra (Fig. S1B) of all the PMA@MIL samples show not only the characteristic bands of MIL-100, but also four notable characteristic bands of PMA located at 1060, 959, 878 and 813 cm^{-1} respectively,[34] revealing the successful introduction of PMA. It is worth noting that with increase of the amount of PMA in the PMA@MIL composite, the relative intensity of the characteristic peaks of PMA increases, though those characteristic peaks shift slightly due to the effect of the complex chemical environment of the MIL-100. Thermogravimetric analysis (TGA) curves of MIL-100 and PMo@MIL-100 samples carried out in air are presented in Fig. S1C. The residual weight of the samples increase with the amount of PMA introduced during the synthesis, indicating more PMA molecules and therefore Mo species were introduced into the PMA@MIL composites.

Nitrogen sorption isotherm curves of the samples measured at 77 K are shown in Fig. S1D and their textural properties are summarized in Table S1. The pristine MIL-100 sample shows the highest BET surface area of 1941 $m^2 g^{-1}$, while the PMA@MIL composites exhibit dramatically decreased surface area with increase the amount of PMA introduced and composite 3-PMA@MIL with the highest PMA content display the lowest specific surface area of 619 $m^2 g^{-1}$. Pore size distribution (Fig. S1E) of the pristine MIL-100 displays a dominated peak at around 2-3 nm, while the PMA@MIL composites exhibit less pores at around 2-3 nm

due to the encapsulation of PMA in the pores of MIL-100. The total pore volumes of PMA@MIL also decrease remarkably compare to that of MIL-100 due to the blockage of pore channels by the encapsulated PMA as well as the added weight from the heavy PMA molecules. Both SEM images (Fig. S2) and TEM images (Fig. S3) of pristine MIL-100 and 1-PMA@MIL do not show any significant difference in morphology and local structure. Moreover, the elemental mappings for pristine MIL-100 and 1-PMA@MIL via TEM (Fig. S4) indicate the homogeneous distribution of all the elements in both samples.

All these results have confirmed that the introduction of PMA to MIL-100 does not change the crystallinity (XRD and FT-IR) and the morphologies (SEM and TEM) of the samples, but affects their textural properties. These PMA@MIL samples are excellent precursors to generate Fe-Mo sulfide/carbon nanocomposites via a simple pyrolysis in H_2S atmosphere at high temperatures.

3.2. Characterisation of the carbon based composite derived from PMA@MIL-100

Fig. 2A shows the XRD patterns of the composites obtained via the pyrolysis of pristine MIL-100 and 1-PMA@MIL in H_2S atmosphere under three different temperatures: 600, 800 and 1000 °C. While the XRD for MIL-100 derived composites exclusively show characteristic diffraction peaks attributed to Fe_7S_8 phase (PDF#71-0647), the XRD patterns for PMA@MIL derived composites are dominated by Fe_7S_8 phase, accompanied with diffraction peaks indexed to MoS_2 phase (PDF#73-1508). Moreover, the XRD of these composites exhibit sharper diffraction peaks at higher sulfurization temperatures, indicating higher sulfurization temperature results in increased crystallinity. It is worth noting that the characteristic (002) peak of MoS_2 in composite 1Mo@MIL-1000 appears at 2θ of 14°, however this characteristic peak in composites 1Mo@MIL-600 and 1Mo@MIL-800 shift to around 11° with broad peak.

This may be due to the incomplete sulfurization of Mo species and the formation of amorphous MoS_2 nanoparticles under lower sulfurization temperatures.

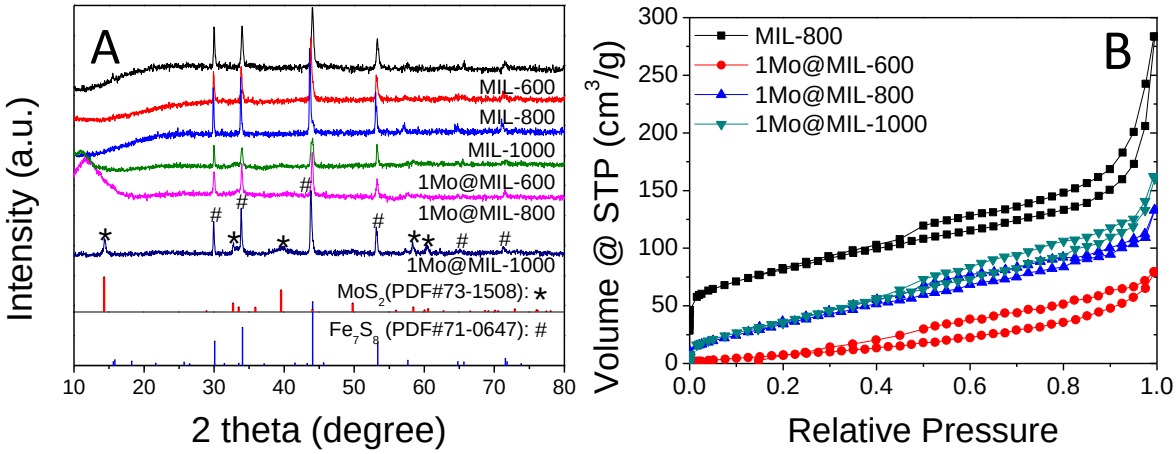

Fig. 2. XRD patterns of A) MIL-600, MIL-800, MIL-1000, 1Mo@MIL-600, 1Mo@MIL-800 and 1Mo@MIL-1000; B) N_2 sorption isotherms of MIL-800, 1Mo@MIL-600, 1Mo@MIL-800 and 1Mo@MIL-1000.

Fig. 2B presents the N_2 sorption isotherms of the PMA modified composites sulfurized at 600, 800 and 1000 °C, and also the sample MIL-100 sulfurized at 800 °C for comparison. All the four samples show type IV isotherms, indicating the formation of mesoporous structure after the sulfurization. 1Mo@MIL-800 possesses a surface area of 141 m^2 g^{-1}, only half of that of MIL-800, likely due to the increased mass of the introduced Mo species. Among the 1-PMA@MIL derived composites, sample 1Mo@MIL-600 sulfurized under 600 °C shows the lowest BET surface area of 39 m^2 g^{-1} and lowest total pore volume of 0.12 cm^3 g^{-1}, possibly owing to the incomplete carbonization of the precursor. However, with the increase of sulfurization temperatures, the resulting composites exhibited enhanced BET surface area and total pore volume (see Table S2). Representative pore size distribution of 1Mo@MIL-800 (Fig.

S5) shows that this material displays a wider size distribution that shifts toward larger pore size compared with the parental 1-PMA@MIL, which may be due to the removal of oxygen and hydrogen from the MOF ligand resulting in the partial collapse of the smaller pores during the sulfurization and carbonization of the MIL-100 framework.

The TEM images of sample 1Mo@MIL-600 which derived from 1-PMA@MIL sulfurized at 600 °C exhibit 2 to 4 atomic layers of MoS_2 crumbs evenly distributed throughout the amorphous carbon matrix (Fig. 3A). Meanwhile it is difficult to identify iron sulfide within the matrix possibly due to its small sizes and homogenously embedded in the formed carbons. Black particles observed on the carbon matrix (see Fig. 3A1 inset) may be the free standing iron species and elemental mapping in Fig. S6A indicates that these particles may be large iron sulfide particles. On the other hand, sample 1Mo@MIL-800 obtained at sulfurization of 800 °C displays thin flakes of 50 nm in diameter and 5-10 layer in thickness (Fig. 3B1) and small onion-like spheres with size around 10 nm (Fig. 3B2) appear, which are evenly embedded in the carbon matrix. At 1000 °C, the flakes become larger in both diameter and thickness (Fig. 3C1). The onion-like spheres also grow larger of size up to 50 nm (Fig. 3C2). By measuring the lattice spacing, it is found that with increase of the sulfurization temperature the d values change from 0.80 to 0.62 nm, which is in line with the wide XRD peak at around 11° of 1Mo@MIL-600/800 (Fig. 2A). Consistent with the pronounce sharp peak at 14° in 1Mo@MIL-1000, a lattice spacing of 0.62 nm is observed in the TEM image (Fig. 3C2), which belongs to the (002) plane of MoS_2. In addition, thin flakes of lighter colour are also observed in both 1Mo@MIL-800/1000 (see Fig. 3B1 and C1). The lattice spacing was shown in the inserts of Fig. 3B2 and C2 and a measured lattice spacing is 0.26 nm, which belongs to the (203) plane of Fe_7S_8, indicating the presence of Fe_7S_8 nanocrystals within the carbon matrix. The TEM elemental mapping of the three samples (Fig. S6) shows that all the elements Fe, Mo, S, C and O are homogeneously distributed throughout the samples.

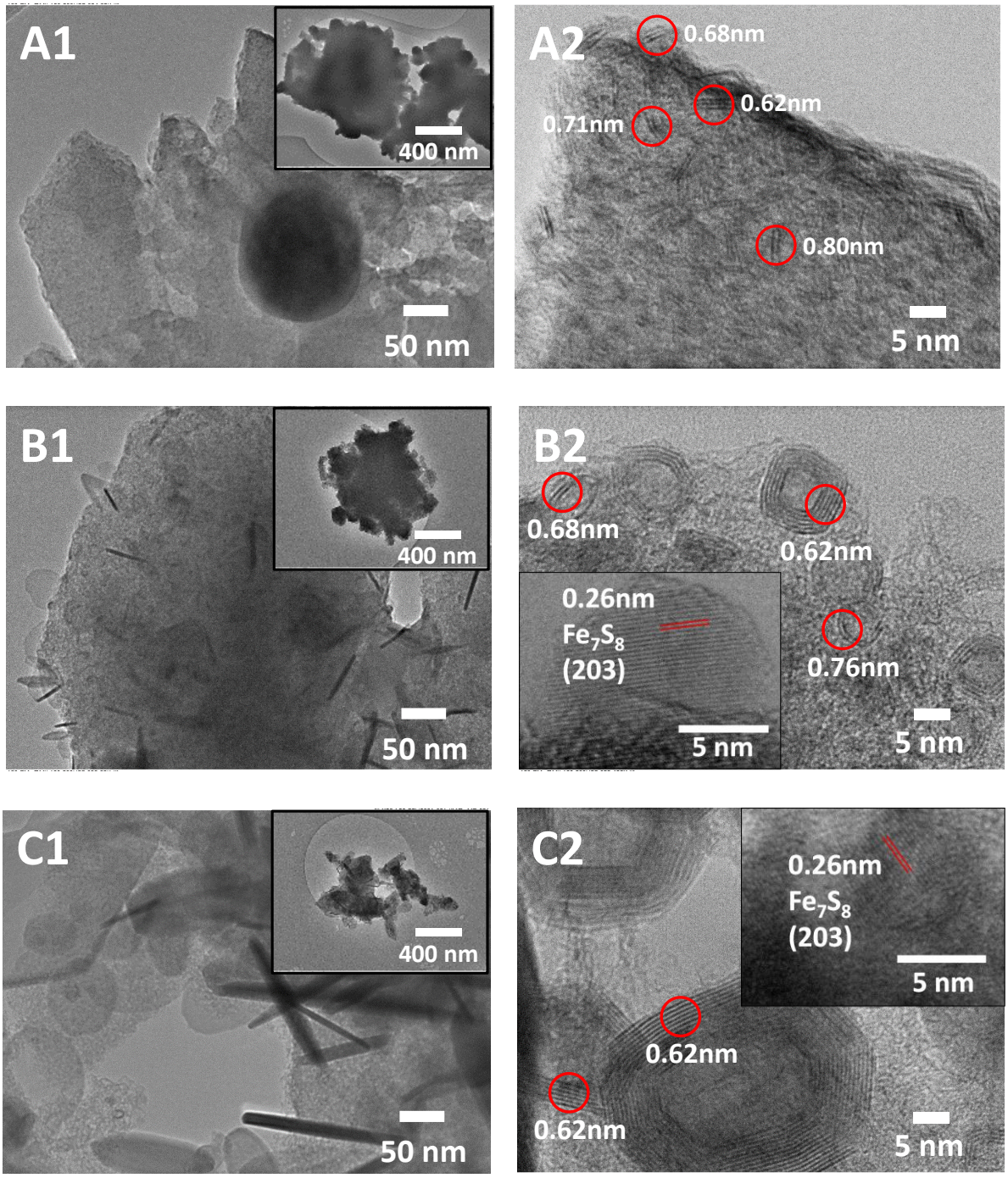

Fig. 3. TEM images of 1-PMA@MIL sulfurized at A) 600°C, B) 800°C and C) 1000°C.

SEM images of the sulfurized MIL-100 and 1-PMA@MIL at 600, 800 and 1000 °C are presented in Fig. 4. In general, all the samples exhibit irregular shaped particle morphologies. The composites derived from both the pristine and the PMA encapsulated precursors at lower

sulfurization temperature show no observable difference in morphology (Fig. 4A and D). However, the SEM image for 1Mo@MIL-800 which was obtained at sulfurization temperature of 800 °C exhibits tiny flakes covered on the surface of the particles resulting in a rough surface (Fig. 4B), while the flakes tended to grow to larger sizes up to 500 nm when the sulfurization temperature increases to 1000 °C (Fig. 4C). In contrast, the samples derived from pristine MIL-100 sulfurized at 800 and 1000 °C do not show any visible flakes on the particle surfaces (Fig. 4E and F). This observation indicates that the thin flakes are likely to be the MoS_2 particles from the sulfurization of PMA under high temperatures, which is consistent with XRD results in Fig. 2A.

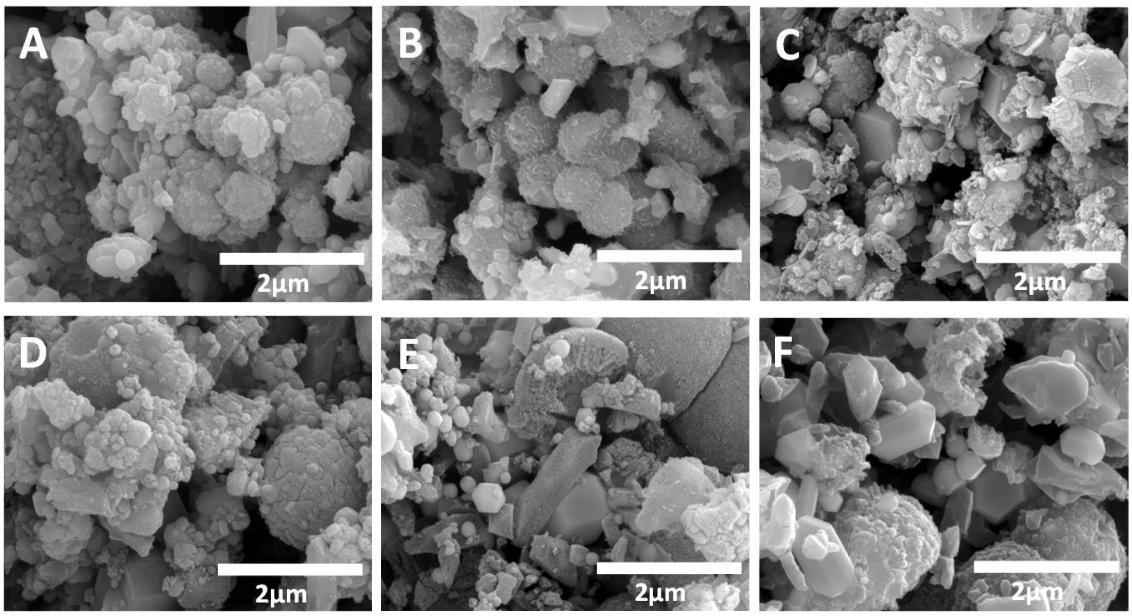

Fig. 4. SEM images of 1-PMA@MIL sulfurized at different temperatures: A) 600 °C, B) 800 °C and C) 1000 °C; and pristine MIL-100 sulfurized at different temperatures D) 600 °C, E) 800 °C and F) 1000 °C.

The elements and their chemical status of samples MIL-800 and 1-PMA@MIL that sulfurized at different temperatures were study by XPS. The element survey spectra inclusively confirm the existence of Fe, O, S and C in all four samples (Fig. 5A), but the 1-PMA@MIL derived samples show the presence of Mo, which is as expected and in good agreement with above XRD and TEM results.

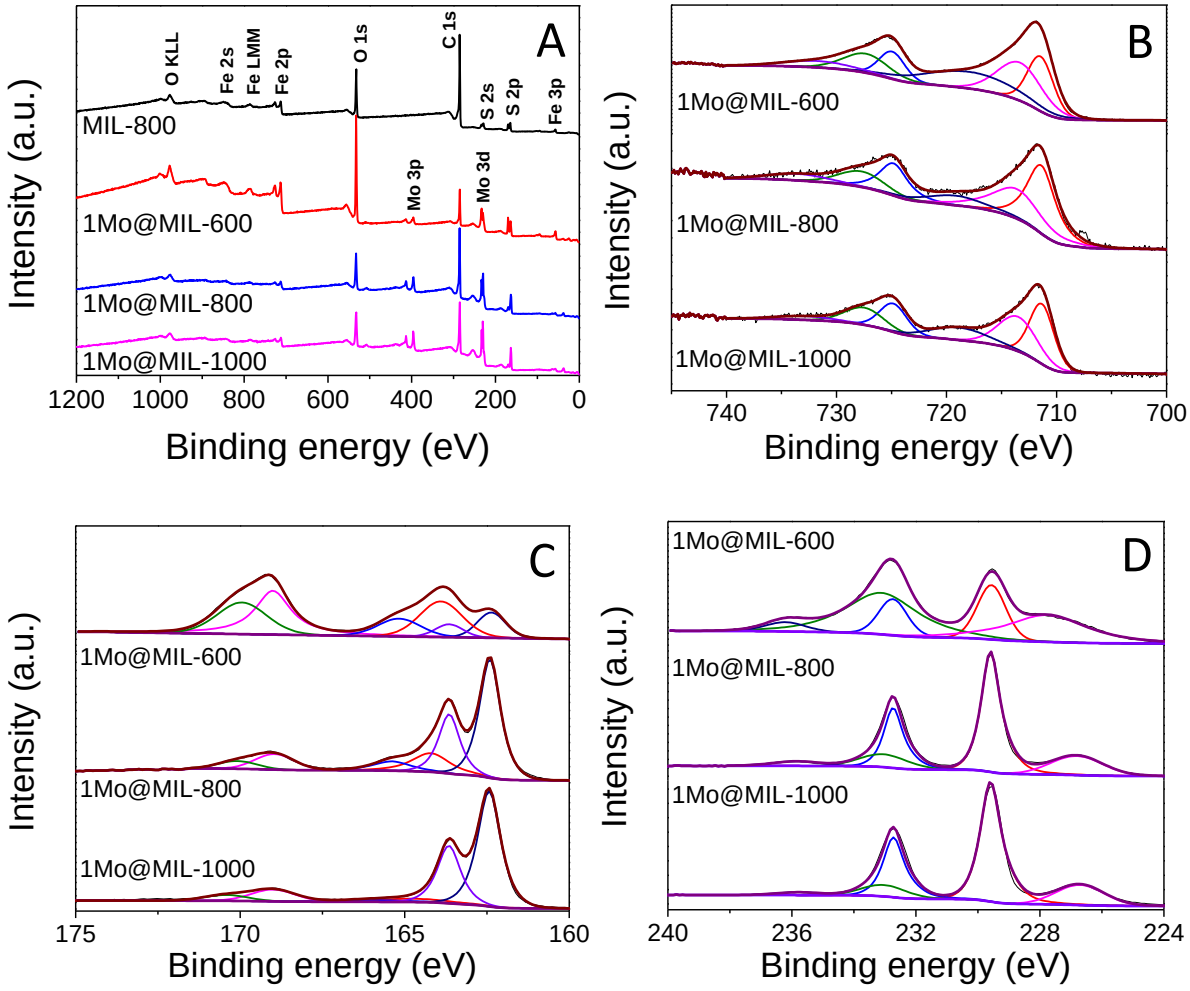

Fig. 5. A) XPS element survey and high-resolution XPS spectra of B) Fe 2p, C) S 2p and D) Mo 3d.

The high-resolution XPS spectra of Fe 2p for the 3 samples derived from the sulfurization of 1-PMA@MIL at different temperatures show two main peaks with each one deconvoluted

into 3 peaks (Fig. 5B). The pair of peaks at around 711.4 and 724.8 eV are attributed to the Fe $2p_{3/2}$ and Fe $2p_{1/2}$ of Fe^{2+} species with 13.4 eV of peak separation,[35, 36] while the other pair of peaks located at around 713.6 and 727.7 eV are ascribed to the Fe $2p_{3/2}$ and Fe $2p_{1/2}$ for Fe^{3+} species.[37-39] The last pair of peaks at around 719.1 and 733.5 eV are the shakeup satellite peaks of Fe $2p_{3/2}$ and Fe $2p_{1/2}$.[38, 39] These results are consistent with previous report.[35] Compared with sample MIL-800, the sample 1Mo@MIL-800 exhibit slightly increase in binding energy of the Fe $2p_{3/2}$ and Fe $2p_{1/2}$ peaks (Fig. S7), suggesting a strong interaction between Fe_7S_8 and MoS_2 particles and the possible formation of Fe-Mo-S species. This will benefit to their catalytic applications since previous reports found that the formation of M-Mo-S phase (M stand for metal such as Co, Ni and Fe) can reduce the energy barriers for the catalytic reaction and enhance the activity toward HER.[9, 40, 41]

The high-resolution S 2p XPS spectra of the three samples derived from 1-PMA@MIL sulfurized at different temperatures is presented in Fig. 5C. The peaks at around 162.4 and 163.6 eV correspond to S $2p_{3/2}$ and S $2p_{1/2}$ of the S^{2-} species, which are originated from the Fe_7S_8 [42] and MoS_2 [43] composition in the composites. In addition, the peaks at around 168.9 and 170.0 eV are the pair signals of the S $2p_{3/2}$ and S $2p_{1/2}$ for SO_x species.[44] It is believed that this is due to the surface oxidation of the samples as well as the possible intermediate product (see previous XRD and TEM analysis) in the sample obtained at lower sulfurization temperature, i.e. 1Mo@MIL-600. Increasing the sulfurization temperatures, the amount of oxidised species in the resulting samples decrease dramatically. The paired S 2p peaks at around 164.2 and 165.3 eV are due to the doping of S species into the carbon matrix in the form of C-S-C and/or C=S respectively.[45] The doping of S in the carbon matrix may introduce active site favourable for HER.[46] However, this doped S species in the composite decrease with the increase of the sulfurization temperature. Actually no doped S species can be identified in sample 1Mo@MIL-1000.

The high-resolution XPS spectra of Mo 3d are shown in Fig. 5D. The first peak at the lower energy end of the spectra is assigned to the S 2s peak due to the overlap region of Mo 3d and S 2s spectra. The intense pair of peaks at around 229.6 and 232.7 eV for all the three samples are originated from Mo $3d_{5/2}$ and Mo $3d_{3/2}$ of Mo^{4+} state in MoS_2.[47] Moreover, two doublets at around 233.0 and 235.8eV in sample 1Mo@MIL-600 are attributed to Mo $3d_{5/2}$ and Mo $3d_{3/2}$ of Mo^{6+} state of the molybdenum species, but those peaks are negligible or virtually disappeared in sample 1Mo@MIL-800 and 1Mo@MIL-1000. Obviously, the intensity of binding energy of those Mo^{6+} species decrease with increased sulfurization temperature,[48] which is, as discussed earlier, possibly due to the surface oxidation of the molybdenum to form intermediate product during the process of MoS_2 generation.

3.3. Electrochemistry performance evaluation

The electrochemical hydrogen revolution reaction (HER) performance of all the samples derived from sulfurized MIL-100 and 1-PMA@MIL under different temperatures are presented in Fig. 6 and relevant HER data are summarized in Table 1. The composite derived from sulfurization of pristine MIL-100 at higher temperatures exhibits improved HER activities in acidic media (Fig. 6A). With the introduction of Mo species, all the three composites derived from the sulfurization of 1-PTA@MIL under different temperatures exclusively show dramatic increase of the onset potential in HER compared to those samples derived from the sulfurized MIL-100 under the same conditions. Moreover, the HER activity of sample 1Mo@MIL-800 is much higher than that of samples 1Mo@MIL-1000 and 1Mo@MIL-600. Actually, sample 1Mo@MIL-800 exhibits the lowest onset potential of -0.241 V (vs. RHE at current density of -1 mA cm^{-2}) and requires the lowest overpotential of -0.321 V (vs. RHE) to achieve the current density of -10 mA cm^{-2}, indicating that 1Mo@MIL-800 composite is the highest HER active sample amongst all the studied composites. It is worth noting that, as shown in the Table 1, the Mo-containing samples 1Mo@MIL-800 and

1Mo@MIL-1000 exhibit remarkable decrease in the onset potential for HER of 0.251 and 0.348 V compared with their Mo-free counterpart MIL-800 and MIL-100 respectively. These results indicate that new catalytic active sites may originate from the introduced MoS_2, the dual metallic Fe-Mo-S phase as well as S-doped carbon (as confirmed in XPS analysis) in the composites, which result in the significant improvement in electrocatalytic HER activities of the bimetallic Fe-Mo sulfide/carbon systems. Nevertheless, the HER performances of these composites are generally still inferior to the benchmark 20% Pt/C sample.

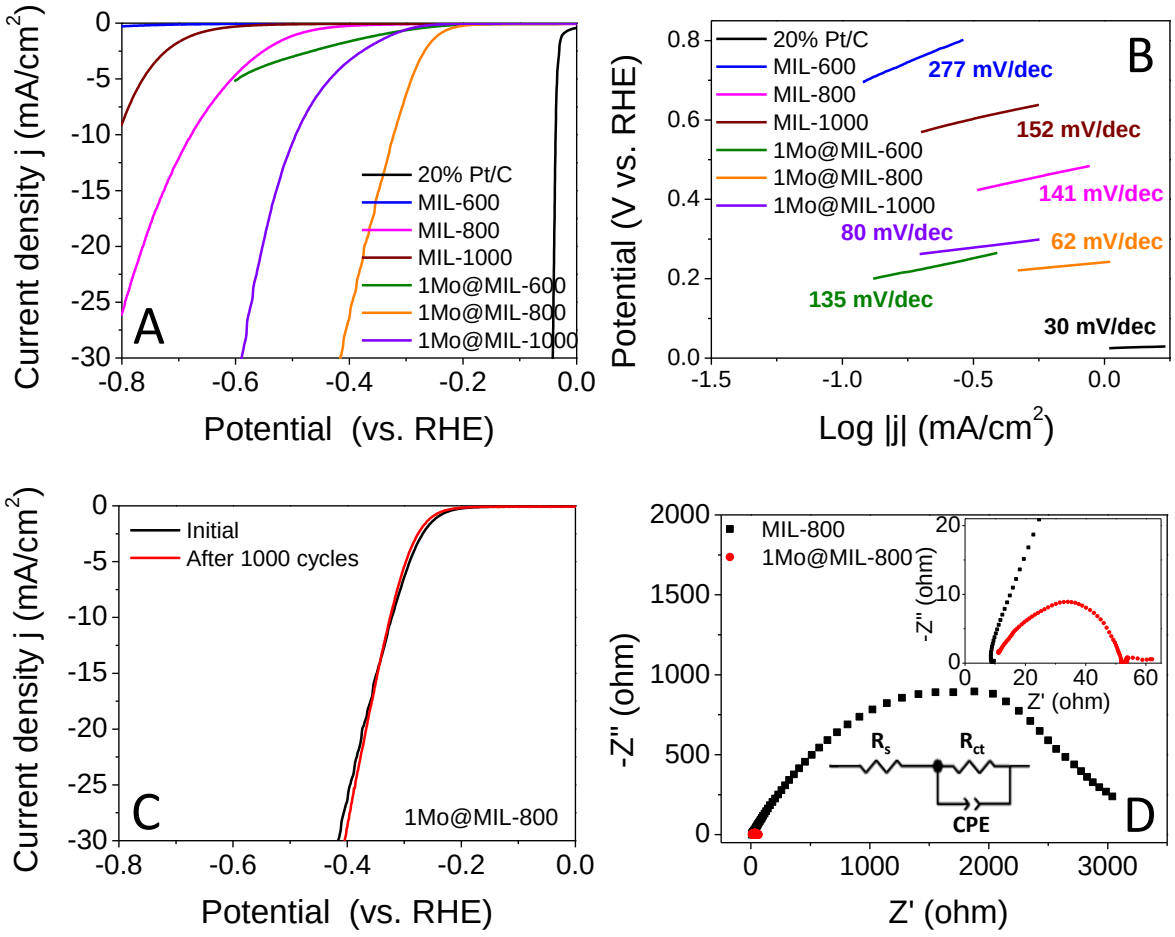

Fig. 6. A) HER polarization curves of MIL-600, MIL-800, MIL-1000 and 1Mo@MIL-600, 1Mo@MIL-800, 1Mo@MIL-1000 and B) The corresponding tafel plots of the samples presented in A). C) Polarization curves of 1Mo@MIL100-800 before and after 1000 cycles and D) EIS of MIL-800 and 1Mo@MIL-800. 0.5 M H_2SO_4 was used as electrolyte, all polarization curves are iR corrected.

Table 1

Summary of the electrochemical HER performance data of different samples.

Sample	Onset potential at -1 mA cm^{-2} (V vs. RHE)	Overpotential at -10 mA cm^{-2} (V vs. RHE)	Tafel slope (mV dec^{-1})
MIL-600	-[1]	-[1]	277
MIL-800	-0.492	-0.678	141
MIL-1000	-0.670	-0.807[2]	152
1Mo@MIL-600	-0.342	-[1]	135
1Mo@MIL-800	-0.241	-0.321	62
1Mo@MIL-1000	-0.322	-0.493	80
20% Pt/C	-0.024	-0.037	30

[1] The current density could not reach -10 mA cm^{-2} within the potential window.

[2] Value obtained by extrapolation of the curve.

Tafel plots that derived from the HER polarization curves of the samples are presented in Fig. 6B and the corresponding values of Tafel slope are labelled in the plots. The three Mo-free samples MIL-600, MIL-800 and MIL-1000 show Tafel slope of 277, 141 and 152 mV dec^{-1} respectively, indicating poor reaction kinetics of these samples. In contrast, all the Mo-containing samples exclusively exhibit much reduced Tafel slope values, suggesting faster reaction kinetics of these bimetallic Fe-Mo sulfide/carbon composites in electrocatalytic HER performance in acidic media. It is interesting to noteworthy that among all the studied composites, samples 1Mo@MIL-800 exhibits the smallest Tafel slope value of 60 mV dec^{-1}, implying the best HER performance amongst all the studied samples. It is widely accepted that a HER process includes Volmer step, Heyrovsky step or Tafel step and both the Volmer-Heyrovsky and the Volmer-Tafel mechanisms lead to the formation of H_2.[49] It is believed that as a rate-determine step, Tafel slope value of ca. 30, 40 and 120 mV dec^{-1} is required for the Tafel step, Heyrovsky step and Volmer step, respectively.[4] Therefore, the HER process

of sample 1Mo@MIL-800 possess a Volmer-Heyrovsky mechanism and the electrochemical recombination is the rate-determination step during the HER process.[50, 51]

For overall water splitting, the performance of the catalyst in different pH media is essential. Therefore, the sample1Mo@MIL-800 with the highest HER activity in acidic media was further evaluated in alkaline and neutral media respectively (Fig. S8). This catalyst needs an overpotential of -0.452 V in 1 M KOH and -0.772 V in 0.5 M Na_2SO_4 to achieve current density of -10 mA cm^{-2}, which is 0.130 V and 0.451 V higher than that in acidic solution. Clearly, HER performance of the composite in acidic solution is better than that of in alkaline or neutral solution. It is also clear that the HER performance of 1Mo@MIL-800 in both alkaline and acid solutions shows a remarkable improvement compared with the Mo-free composite MIL-800 under the same conditions.

It was reported that when Pt is used as the counter electrode during the HER test, it could transfer to the working electrode and affects the catalytic performance of the measured sample,[52] we therefore validated the HER test of the best performed sample, 1Mo@MIL-800 using graphite rod instead of Pt wire as the counter electrode. As shown in Fig. S9, there is no obvious difference of the HER performance when using graphite rod as counter electrode, compared with the use of Pt wire electrode. Even after 1000 cycles test using the graphite rod as counter electrode, the HER performance of the composite largely remains unchanged, indicating the use of different counter electrodes has negligible effect on the elctrocatalytic performance of the composite.

The stability of the best performed composite 1Mo@MIL-800 in HER was evaluated by comparing the LSV curves before and after 1000 cycles of measurements. The result in Fig. 6C shows a negligible decay of current density after 1000 cycles of HER tests, indicating very good stability of this composite. Moreover, the time dependence on current curve of this sample

(Fig. S10) displays that the current density only decrease slightly after 8000 s of testing in HER, suggesting a good stability of the catalyst under the studied constant voltage.

The electrochemical impedance spectroscopy (EIS) of 1Mo@MIL-800 was further analyzed in the frequency range of 10^6 to 0.1 Hz at -0.6 V (vs. RHE) and the EIS of MIL-800 was also included for comparison. The Nyquist plots in Fig. 6D exhibit semi-circle shapes and both samples can be modelled by an electric circuit consist of a series resistance (R_s), a constant phase element (CPE) and a charge-transfer resistance (R_{ct}) as shown in the insert of Fig. 6D. The value of R_{ct} can be calculated from the diameter of the semi-circle at high frequency in the Nyquist plot, and the smaller the value of R_{ct}, the higher the charge transfer rate, therefore the faster the interfacial kinetics and the better performance of the composite. Based on the curve fitting, the value of R_{ct} for sample 1Mo@MIL-800 is 48 Ω which is much smaller than that of sample MIL-800 (3491 Ω), indicating that the presence of MoS_2 generates catalytically active sites and the formation of Fe-Mo-S species in the composite dramatically promote faster interfacial kinetics.[53]

As discussed above, the pyrolysis temperatures of the precursor remarkably affect the HER performance of the resulting materials. Other parameters such as the amount of PMA in the precursor, the heating ramp rate to the sulfurization temperature and the sulfurization duration that can potential influence on the electrocatalytic HER activities of the resulting materials were also explored.

The effect of the amount of PMA in the precursor on the XRD patterns of the composites obtained via pyrolysis of pristine MIL-100 and PMA@MIL at 800 °C in H_2S atmosphere was presented in Fig. 7A. While MIL-800 only exhibits the diffraction peaks that can be indexed to iron sulfide phase like Fe_7S_8 (PDF#71-0647), all the three composites derived from PMA@MIL with different PMA content show characteristic peaks that are indexed to Fe_7S_8

and MoS_2 (PDF#73-1508), suggesting the formation of Fe-Mo bimetallic sulfides in the composites. Moreover, the relative intensity of the peaks indexed to MoS_2 phase in the composites increases with the amount of introduced PMA in the precursor. While the characteristic (002) peak of MoS_2 phase in composite 3Mo@MIL-800 and 2Mo@MIL-800 that derived from higher PMA content precursor appears at 2ϑ of 14º, but the characteristic peaks in composite 1Mo@MIL-800, which is derived from lower PMA content precursor, shifts to lower 2ϑ range of 11º with broader peak. In addition, element content obtained from SEM-EDX also confirmed that with the increased amount of PMA introduced into the precursor, the resulting sample Mo@MIL-800 exhibited increased Mo content in the composites (Table S3).

The HER performance of the composites with variable molybdenum content in the Mo@MIL-800 samples are also evaluated and presented in Fig. 7B. It is obvious that with the increase of the Mo content in Mo@MIL-800 composites, their catalytic activities actually decrease. The overpotential to achieve current density of -10 mA cm^{-2} decreases from -0.321 V for sample 1Mo@MIL-800 to –0.482 V for sample 3Mo@MIL-800, and the Tafel slope value increases from 60 mV dec^{-1} for sample 1Mo@MIL-800 to 127 mV dec^{-1} for sample 3Mo@MIL-800,which almost doubles the value of 1Mo@MIL-800 composite. These results imply that the increased amount of Mo content in the Mo@MIL-800 composites deteriorates their HER performance, which may be due to the agglomeration of MoS_2 at higher amount, leading to the hindering of the access to the catalytic active sites in the composite.

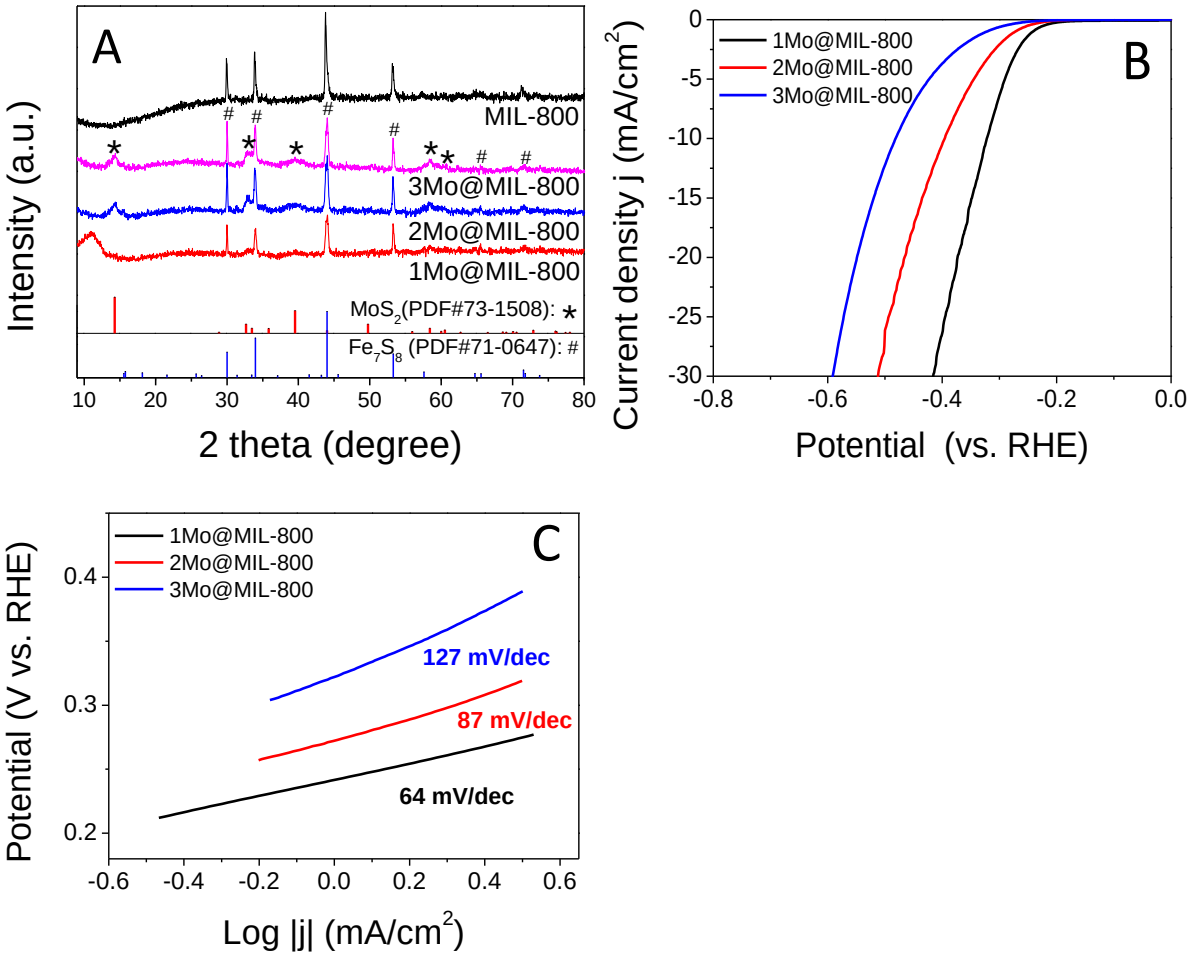

Fig. 7. A) Power XRD patterns, B) HER performance and C) the corresponding Tafel plots of Mo@MIL-800 with variable Mo content. In the HER measurement in B), 0.5 M H_2SO_4 was used as electrolyte, and all polarization curves are iR corrected.

The effect of heat ramp rate to the sulfurization temperature and the sulfurization duration on the electrocatalytic performances of the samples have also been studied. Fig. S11A and B show the XRD patterns of samples obtained at different heating ramp rates (10 or 2 °C min^{-1}) and sulfurization time (20 min or 2 h in H_2S gas, or 1 h in Ar followed by 1 h in H_2S). All samples exclusively exhibit XRD diffraction peaks indexed to both Fe_7S_8 and MoS_2 phases. With slower heating ramp rate, the diffraction peaks for MoS_2 become more pronounce and the broader peak at lower 2θ angle disappears, indicating a better crystallinity and well

established MoS_2 lattice structure under slow heating ramp rate. As for the effect of sulfurization time on the XRD patterns of resulting samples, there is no visible difference between the sample obtained in H_2S for 2 h and the one in Ar for 1 h followed by in H_2S for 1 h. However, the sample sulfurized for only 20 min in H_2S shows a broad peak at lower 2θ angle, suggesting the incomplete sulfurization of Mo species and the formation of amorphous MoS_2 nanoparticles.

The HER polarization curves (Fig. S11C) indicate that the sample obtained via slower heating rate exhibits slightly inferior HER performance than the sample prepared from faster heating ramp rate. This is possible due to the fact that eletrocatalytic HER active sites are located on the defects and exposed edges of metal sulphides,[4] and a slower heating rate provides higher opportunities for the metal sulfides to establish its crystallinity,[54] which result in less exposed active sites and consequently unsatisfactory HER performance. On the other hand, the change of sulfurization time does not cause significant difference in the HER performance (Fig. S11D), indicating that the sulfurization time is not a major factor that affects the electrocatalytic HER activity of the composites.

4. Conclusions

In summary, we have successfully fabricated bimetallic Fe-Mo sulfide/S-doped carbon nanocomposites from PMA@MIL precursors. Nanosized metal sulfide crystals are homogeneously embedded in the porous carbon matrix, leading to significant improvement in HER activities under acidic condition. In particular, composite 1Mo@MIL-800 exhibits an overpotential of -0.321V to realise current density of -10 mA cm^{-2} and a Tafel slope of 62 mV dec^{-1}, which shows a 53% reduction in overpotential to achieve the same current density compared with Mo-free composite MIL-800. This dramatic improvement in HER performance

of the PMA@MIL derived nanocomposites can be attributed to: (1) large amount of active sites are introduced by the evenly distributed nanosized MoS_2 throughout the carbon matrix; (2) strong interactions are formed between the two metallic sulfides, forming Fe-Mo-S phases that are favourable for HER and (3) more HER active site have been created by S-doping in the carbon matrix. Moreover, the Fe-Mo sulfide/carbon composites are electrocataytic active for HER not only in acidic media, but also in alkaline and neutral media. In addition, It was also found that although the sulfurization time of the composites does not affect the HER performance, both higher Mo amount and higher heating ramp rate for the composites lead to deteriorated HER performance. This work offers a feasible way to generate complex heterogeneous electrocatalyic composites with great potential for diverse applications.

Acknowledgements

This work was support by EPSRC Doctoral Training Partnership at University of Exeter, Leverhulme Trust (RPG-2018-320) and EU RFCS (RFCS-2016-754077) are greatly acknowledged.

Appendix A. Supplementary data

The following is Supplementary data to this article:

References

[1] D.G.M. Vladimir A. Blagojević, Jasmina Grbović Novaković and Dragica M. Minic, Hydrogen Economy: Modern Concepts, Challenges and Perspectives, in: D. Minic (Ed.), Hydrogen Energy-Challenges and Perspectives, IntechOpen, IntechOpen, 2012.

[2] X. Zou, Y. Zhang, Chem. Soc. Rev. 44(15) (2015) 5148-5180.

[3] L. Liu, A. Corma, Chem. Rev. 118(10) (2018) 4981-5079.

[4] J.D. Benck, T.R. Hellstern, J. Kibsgaard, P. Chakthranont, T.F. Jaramillo, ACS Catal. 4(11) (2014) 3957-3971.

[5] Y. Huang, Y. Sun, X. Zheng, T. Aoki, B. Pattengale, J. Huang, X. He, W. Bian, S. Younan, N. Williams, J. Hu, J. Ge, N. Pu, X. Yan, X. Pan, L. Zhang, Y. Wei, J. Gu, Nat. Commun. 10(1) (2019) 982.

[6] T. Li, G. Galli, J. Phys. Chem. C 111(44) (2007) 16192-16196.

[7] T.F. Jaramillo, K.P. Jørgensen, J. Bonde, J.H. Nielsen, S. Horch, I. Chorkendorff, Science 317(5834) (2007) 100-102.

[8] B. Hinnemann, P.G. Moses, J. Bonde, K.P. Jørgensen, J.H. Nielsen, S. Horch, I. Chorkendorff, J.K. Nørskov, J. Am. Chem. Soc. 127(15) (2005) 5308-5309.

[9] D. Merki, H. Vrubel, L. Rovelli, S. Fierro, X. Hu, Chem. Sci. 3(8) (2012) 2515-2525.

[10] J. Deng, H. Li, S. Wang, D. Ding, M. Chen, C. Liu, Z. Tian, K.S. Novoselov, C. Ma, D. Deng, X. Bao, Nat. Commun. 8(1) (2017) 14430.

[11] Y. Shi, Y. Zhou, D.-R. Yang, W.-X. Xu, C. Wang, F.-B. Wang, J.-J. Xu, X.-H. Xia, H.-Y. Chen, J. Am. Chem. Soc. 139(43) (2017) 15479-15485.

[12] M. Hakala, R. Kronberg, K. Laasonen, Sci. Rep. 7(1) (2017) 15243.

[13] C. Di Giovanni, W.-A. Wang, S. Nowak, J.-M. Grenèche, H. Lecoq, L. Mouton, M. Giraud, C. Tard, ACS Catal. 4(2) (2014) 681-687.

[14] C.D. Giovanni, Á. Reyes-Carmona, A. Coursier, S. Nowak, J.M. Grenèche, H. Lecoq, L. Mouton, J. Rozière, D. Jones, J. Peron, M. Giraud, C. Tard, ACS Catal. 6(4) (2016) 2626-2631.

[15] S. Chen, Z. Kang, X. Zhang, J. Xie, H. Wang, W. Shao, X. Zheng, W. Yan, B. Pan, Y. Xie, ACS Cent. Sci. 3(11) (2017) 1221-1227.

[16] Y. Guo, C. Shang, X. Zhang, E. Wang, Chem. Commun. 52(79) (2016) 11795-11798.

[17] H. Wang, C. Tsai, D. Kong, K. Chan, F. Abild-Pedersen, J.K. Nørskov, Y. Cui, Nano Res. 8(2) (2015) 566-575.

[18] X. Zhao, X. Ma, Q. Lu, Q. Li, C. Han, Z. Xing, X. Yang, Electrochim. Acta 249 (2017) 72-78.

[19] S. Chen, S. Huang, J. Hu, S. Fan, Y. Shang, M.E. Pam, X. Li, Y. Wang, T. Xu, Y. Shi, H.Y. Yang, Nano-Micro Lett. 11(1) (2019) 80.

[20] Y. Guo, Z. Yao, B.J.J. Timmer, X. Sheng, L. Fan, Y. Li, F. Zhang, L. Sun, Nano Energy 62 (2019) 282-288.

[21] G. Férey, C. Mellot-Draznieks, C. Serre, F. Millange, J. Dutour, S. Surblé, I. Margiolaki, Science 309(5743) (2005) 2040-2042.

[22] D.-Y. Du, J.-S. Qin, S.-L. Li, Z.-M. Su, Y.-Q. Lan, Chem. Soc. Rev. 43(13) (2014) 4615-4632.

[23] C. Romain, R.-M. Catherine, H. Mohamed, V. Alexandre, H. Patricia, S. Francis, S. Christian, Curr. Inorg. Chem. 7(2) (2017) 145-156.

[24] P. Horcajada, S. Surblé, C. Serre, D.-Y. Hong, Y.-K. Seo, J.-S. Chang, J.-M. Grenèche, I. Margiolaki, G. Férey, Chem. Commun. (27) (2007) 2820-2822.

[25] Q. Lan, Z.-M. Zhang, C. Qin, X.-L. Wang, Y.-G. Li, H.-Q. Tan, E.-B. Wang, Chem. Eur. J. 22(43) (2016) 15513-15520.

[26] J.-S. Li, Y.-J. Tang, C.-H. Liu, S.-L. Li, R.-H. Li, L.-Z. Dong, Z.-H. Dai, J.-C. Bao, Y.-Q. Lan, J. Mater. Chem. A 4(4) (2016) 1202-1207.

[27] H.B. Wu, B.Y. Xia, L. Yu, X.-Y. Yu, X.W. Lou, Nat. Commun. 6(1) (2015) 6512.

[28] Y.-J. Tang, M.-R. Gao, C.-H. Liu, S.-L. Li, H.-L. Jiang, Y.-Q. Lan, M. Han, S.-H. Yu, Angew. Chem. Int. Ed. 54(44) (2015) 12928-12932.

[29] Z. Huang, Z. Yang, M.Z. Hussain, B. Chen, Q. Jia, Y. Zhu, Y. Xia, Electrochim. Acta 330 (2020) 135335.

[30] C. Wu, J. Hu, J. Tian, F. Chu, Z. Yao, Y. Zheng, D. Yin, C. Li, ACS Appl. Mater. Interfaces 11(6) (2019) 5966-5977.

[31] Z.P. Shi, Y.X. Wang, H.L. Lin, H.B. Zhang, M.K. Shen, S.H. Xie, Y.H. Zhang, Q.S. Gao, Y. Tang, J. Mater. Chem. A 4(16) (2016) 6006-6013.

[32] R. Canioni, C. Roch-Marchal, F. Sécheresse, P. Horcajada, C. Serre, M. Hardi-Dan, G. Férey, J.-M. Grenèche, F. Lefebvre, J.-S. Chang, Y.-K. Hwang, O. Lebedev, S. Turner, G. Van Tendeloo, J. Mater. Chem. 21(4) (2011) 1226-1233.

[33] R. Liang, R. Chen, F. Jing, N. Qin, L. Wu, Dalton Trans. 44(41) (2015) 18227-18236.

[34] W. Sun, Y. Si, H. Jing, Z. Dong, C. Wang, Y. Zhang, L. Zhao, W. Feng, Y. Yan, Chem. Res. Chin. Uni. 34(3) (2018) 464-469.

[35] W. Chen, X. Zhang, L. Mi, C. Liu, J. Zhang, S. Cui, X. Feng, Y. Cao, C. Shen, Adv. Mater. 31(8) (2019) 1806664.

[36] J. Yang, X. Wang, B. Li, L. Ma, L. Shi, Y. Xiong, H. Xu, Adv. Funct. Mater. 27(17) (2017) 1606497.

[37] Y. Ding, Y. Niu, J. Yang, L. Ma, J. Liu, Y. Xiong, H. Xu, Small 12(39) (2016) 5414-5421.

[38] T. Szatkowski, M. Wysokowski, G. Lota, D. Pęziak, V.V. Bazhenov, G. Nowaczyk, J. Walter, S.L. Molodtsov, H. Stöcker, C. Himcinschi, I. Petrenko, A.L. Stelling, S. Jurga, T. Jesionowski, H. Ehrlich, RSC Adv. 5(96) (2015) 79031-79040.

[39] P.M. Hallam, M. Gómez-Mingot, D.K. Kampouris, C.E. Banks, RSC Adv. 2(16) (2012) 6672-6679.

[40] A.C. Domask, R.L. Gurunathan, S.E. Mohney, J. Electron. Mater. 44(11) (2015) 4065-4079.

[41] Y.-J. Tang, A.M. Zhang, H.-J. Zhu, L.-Z. Dong, X.-L. Wang, S.-L. Li, M. Han, X.-X. Xu, Y.-Q. Lan, Nanoscale 10(18) (2018) 8404-8412.

[42] Q. Zhang, J. Liao, M. Liao, J. Dai, H. Ge, T. Duan, W. Yao, Appl. Surf. Sci. 473 (2019) 799-806.

[43] D. Zhang, B. Li, S. Wang, S. Yang, ACS Appl. Mater. Interfaces 9(46) (2017) 40265-40272.

[44] Z. Liu, F. Wang, M. Li, Z.-H. Ni, RSC Adv. 6(44) (2016) 37500-37505.

[45] Y. Zhou, Y. Leng, W. Zhou, J. Huang, M. Zhao, J. Zhan, C. Feng, Z. Tang, S. Chen, H. Liu, Nano Energy 16 (2015) 357-366.

[46] Y. Tian, Z. Wei, X. Wang, S. Peng, X. Zhang, W.-m. Liu, Int. J. Hydrogen Energy 42(7) (2017) 4184-4192.

[47] G. Tai, T. Zeng, J. Yu, J. Zhou, Y. You, X. Wang, H. Wu, X. Sun, T. Hu, W. Guo, Nanoscale 8(4) (2016) 2234-2241.

[48] P. Qin, G. Fang, W. Ke, F. Cheng, Q. Zheng, J. Wan, H. Lei, X. Zhao, J. Mater. Chem. A 2(8) (2014) 2742-2756.

[49] M.-L. Grutza, A. Rajagopal, C. Streb, P. Kurz, Sustain. Energy Fuels 2(9) (2018) 1893-1904.

[50] L. Ma, L.R.L. Ting, V. Molinari, C. Giordano, B.S. Yeo, J. Mater. Chem. A 3(16) (2015) 8361-8368.

[51] X. Xiao, D. Huang, Y. Fu, M. Wen, X. Jiang, X. Lv, M. Li, L. Gao, S. Liu, M. Wang, C. Zhao, Y. Shen, ACS Appl. Mater. Interfaces 10(5) (2018) 4689-4696.

[52] G. Dong, M. Fang, H. Wang, S. Yip, H.-Y. Cheung, F. Wang, C.-Y. Wong, S.T. Chu, J.C. Ho, J. Mater. Chem. A 3(24) (2015) 13080-13086.

[53] S.H. Yu, D.H.C. Chua, ACS Appl. Mater. Interfaces 10(17) (2018) 14777-14785.

[54] J. Zhang, F. Meng, R.I. Todd, Z. Fu, Scripta Mater. 62(9) (2010) 658-661.